

Observation of an anomaly in the statistics of Kibble-Zurek defects

Jan Balewski^{†,1,*} Alexey Khudorozhkov^{†,2,3,*} Siva Darbha,¹ Omar A. Ashour,^{1,4} Fangli Liu,² Eral Rrapaj,¹ Sheng-Tao Wang,² Pedro L. S. Lopes,² Katherine Klymko^{†,1} Milan Kornjača^{†,2} and Daan Camps^{†1}

¹*National Energy Research Scientific Computing Center,*

Lawrence Berkeley National Laboratory, Berkeley, CA 94720, USA

²*QuEra Computing Inc., 1284 Soldiers Field Road, Boston, MA, 02135, USA*

³*Department of Physics, Boston University, Boston, MA 02215, USA*

⁴*Department of Physics, University of California, Berkeley, California 94720, USA*

(Dated: December 3, 2025)

The Kibble-Zurek mechanism quantifies defect formation during adiabatic passage across a continuous phase transition, providing key insights into universality in quantum many-body systems. We explore counting statistics of defects in adiabatic passage experiments on long 1D Rydberg atom chains. The experiments reveal an anomaly in the defect number distribution at long ramp times, challenging the hypothesis of defect formation through independent domain mergers. Numerical simulations confirm the anomaly and suggest its link to non-critical coarsening dynamics, which we suppress in prepare-and-hold experiments. Our results highlight the ability of quantum simulators to uncover unexpected correlated quantum phenomena.

The Kibble-Zurek (KZ) [1–3] mechanism describes universal topological defect dynamics for a system driven across a continuous phase transition at a finite rate. As the control parameter approaches criticality, the diverging relaxation time causes the dynamics to “freeze out”, producing a characteristic scaling $\langle D \rangle \propto \Gamma^{-\mu}$ of the mean defect density $\langle D \rangle$ with the ramp rate Γ , where μ is determined solely by equilibrium critical exponents. The KZ mechanism has been verified experimentally across systems ranging from liquid crystals to superconductors to ultracold gases, establishing a central paradigm in nonequilibrium statistical mechanics [4–11]. In quantum systems, Rydberg atom arrays have emerged as powerful probes of phase-transition dynamics: experiments have observed universal KZ scaling in one- and two-dimensional Ising transitions, explored real-time dynamics across quantum critical points and phases, and revealed non-critical coarsening that persists long after crossing a transition [12–17]. These experiments have extended KZ studies from measuring the average defect number scaling towards resolving defect correlations in a tunable setting.

While the mean density of excitations satisfies KZ scaling, the statistics of defect formation could encode richer information. Recent theoretical studies have proposed, however, that all cumulants of the defect counting distribution scale universally with the same KZ exponent [18–23]. The results follow from an “independent-domain-merger” picture [Fig. 1(a)]: as the system approaches criticality, pre-domains nucleate on length scales set by

the Kibble-Zurek correlation length ξ . These domains merge without a topological defect only when their ordering is compatible. Assuming that the merges are independent and random, the defect formation is naturally modeled as a Poisson-binomial process. As a direct consequence, all moments of the defect counting distribution, notably the variance, are proportional to, and smaller than, the mean, thereby reproducing KZ scaling.

This hypothesis was inspired by studies in integrable models [18], where free quasiparticles enforce the independent-domain-merger picture, and has proven remarkably successful. Experiments on quantum annealers and superconducting qubit processors have reported defect statistics consistent with the theoretical expectations for integrable models, reinforcing the view that defect formation reflects uncorrelated domain mergers [10, 24, 25]. Yet these successes raise a fundamental question: does the counting statistics universality based on the independent-domains assumption remain valid in more ubiquitous non-integrable, short-ranged, strongly-interacting quantum systems [26–29]?

In this letter, we find that the universality of defect statistics is violated in a non-integrable quantum system. Using Rydberg chains with up to 58 atoms, we measure the full counting statistics of KZ defects across the \mathbb{Z}_2 phase transition, observing timescale-dependent behavior. In faster ramps, we find statistics consistent with the Poisson-binomial predictions of the independent-defect picture. However, in slower ramps, we observe a remarkable anomaly: the variance of the defect count-

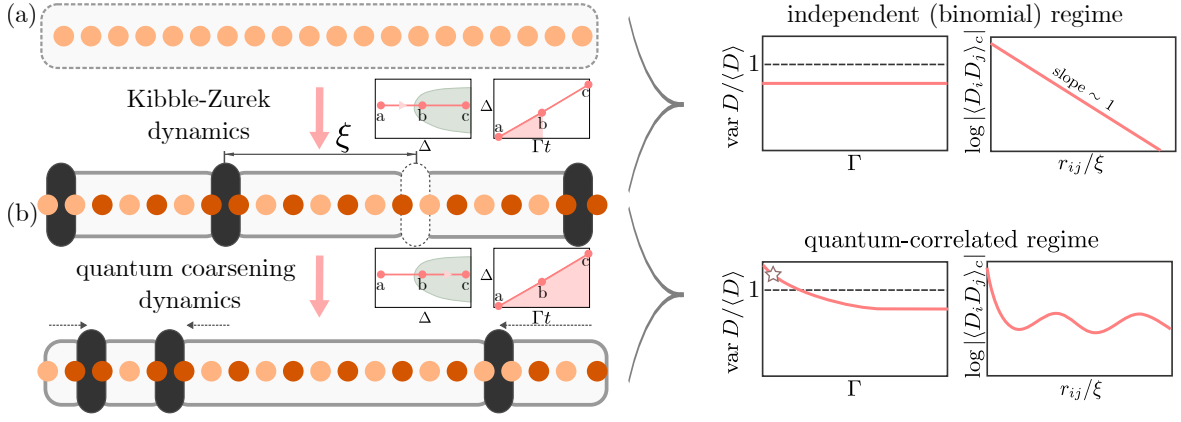


FIG. 1. **Kibble-Zurek defect formation and statistics anomaly.** (a) Schematic of a Rydberg atom array with Ising spins (orange/brown dots). As the system is driven from a paramagnetic phase ‘a’ through the vicinity of a critical point ‘b’ into the antiferromagnetic phase, pre-domains of antiferromagnetic order develop on a correlation length (ξ) scale. The mergers between the domains result in the formation (black) or absence (white) of the domain wall defect at random. This results in the Poisson-binomial defect counting statistics at time point ‘b’, with variance proportional to, and smaller than, the mean, and uncorrelated defects (top right). (b) For slow driving rates Γ , we observe that defects become correlated through coarsening dynamics deep within the antiferromagnetic phase lobe, ‘c’, resulting in a defect counting statistics anomaly (bottom right).

ing statistics exceeds the mean, deviating from universal scaling, and the defect distribution becomes super-Poissonian. Exact-diagonalization simulations reproduce this anomaly and reveal a connection with long-range defect-defect correlations. We attribute the anomaly in defect statistics, and the development of defect correlations, to post-critical coarsening [15, 30–32] [Fig. 1(b)]. Finally, we suppress such coarsening in prepare-and-hold experiments, finding a phenomenology in sharp contrast to recent two-dimensional results [15], thus opening a new line of inquiry.

We explore defect statistics using the Aquila [33, 34] Rydberg atom quantum simulator, which operates the coherent dynamics of Rubidium arrays under the Rydberg Hamiltonian

$$\frac{\mathcal{H}(t)}{\hbar} = \frac{\Omega(t)}{2} \sum_j (|g_j\rangle\langle r_j| + |r_j\rangle\langle g_j|) - \Delta(t) \sum_j n_j + C_6 \sum_{j < k} \frac{n_j n_k}{|\vec{r}_j - \vec{r}_k|^6}, \quad (1)$$

with j indexing the atoms arranged in a chain with nearest neighbor distance a . $\Omega(t)$ and $\Delta(t)$ are, respectively, the Rabi frequency and detuning coupling the ground states $|g_j\rangle$ and highly-excited Rydberg states $|r_j\rangle$, with excited state population $n_j = |r_j\rangle\langle r_j|$. The strong Van der Waals interactions between excited atoms lead to the effective Rydberg blockade, whereby simultaneous excitations of atoms within the radius $R_b = (C_6/\Omega)^{1/6}$ are strongly suppressed.

The Rydberg Hamiltonian is non-integrable, with its ground state phase diagram studied extensively in experiments [12, 13, 35]. We focus on the first-neighbor blockade regime $R_b/a \in [1, 2]$. At low detuning, the ground state of the system is paramagnetic, adiabatically con-

nected to the all-ground product state. At high detuning, the system is in an antiferromagnetic phase, adiabatically connected to the product state with the maximum number of Rydberg excitations consistent with the first neighbor blockade. A quantum critical transition in the \mathbb{Z}_2 universality class separates the two phases [36, 37], characterized by $\mu = 0.5$ Kibble-Zurek scaling exponent, probed previously in Ref. [13]. This transition is used in our experiments to probe the counting statistics of defects and test the independent-defect theory in the non-integrable setting.

To facilitate experiments at scale, we arrange 58 atoms in a loop-chain configuration [Fig. 2(a)] consistent with experimental spacing constraints [33]. We perform a series of adiabatic preparation experiments characterized by the Rabi drive $\Omega(t)$ with its maximal value yielding $R_b/a = 1.35$, while linearly ramping the detuning $\Delta(t)$ from large negative values, through the \mathbb{Z}_2 transition [12] [Fig. 2(b)], to a constant final value well within the antiferromagnetic phase. The detuning ramp duration, t_Δ , controls the rate, $\Gamma = (\Delta_{\max} - \Delta_{\min})/t_\Delta$, at which the transition is crossed. The experimental constraints enable a sizable dynamic range, $\Gamma/2\pi \in (2, 70)$ MHz/ μ s. For each value of t_Δ , we collect 2000 measurement shots, retaining approximately 75% after postselecting for defectless initial atoms placement.

We first measure the correlation length of the adiabatically prepared states, ξ and its dependence on the ramping rate by estimating the expectation value of the density-density correlations and fitting them to exponential decay, $|\langle n_i n_{i+l} \rangle| \propto e^{-l/\xi}$. The correlation length fits for several characteristic ramping rate values are presented in Fig. 2(c), showing a clear trend towards higher correlation length with slower ramps. Even though the readout error, significant in this analog simulator [33],

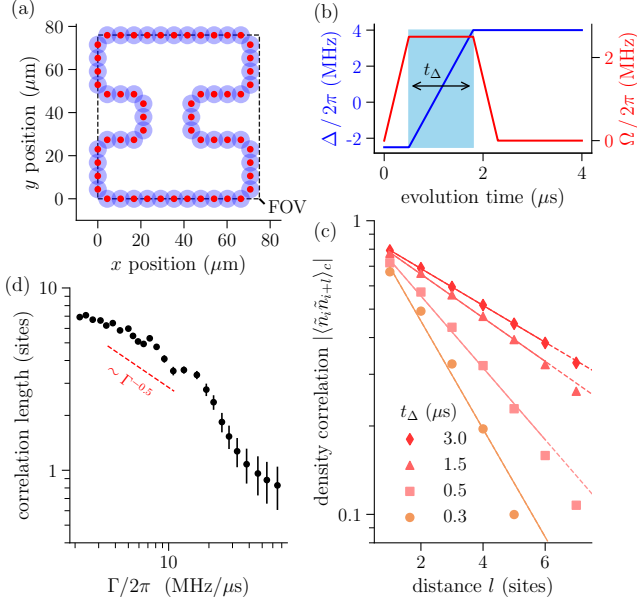


FIG. 2. Experimental setup and correlation length measurement. (a) The 58 atom geometry chosen to fit in the Aquila simulator [33] field of view. Red circles indicate the atom positions separated by $a = 6.2 \mu\text{m}$, and semi-transparent blue circles show blockade radii $R_b/a = 1.35$. (b) The Rabi frequency $\Omega(t)$ and detuning $\Delta(t)$ drives used to adiabatically prepare ground states of the antiferromagnetic phase. The blue shaded region shows the variable detuning ramp time $t_\Delta \in [0, 3] \mu\text{s}$. (c) The two-point Rydberg density correlations $|\langle \tilde{n}_i \tilde{n}_{i+l} \rangle_c|$ ($\tilde{n} = n - 1/2$) as a function of distance l for different ramp times. The solid lines show exponential fits over $l \in [1, 6]$ used to extract correlation lengths. (d) The defect correlation length vs the quench rate Γ . For intermediate-ramp-rate quenches, the behavior approaches the expected $\mu = 0.5$ Kibble-Zurek scaling (red line).

affects the correlation functions, the effect is uniform across displacement l , making correlation length estimation based on fitting robust [38]. The scaling of the correlation length across the accessible range of ramping rates [Fig. 2(d)] establishes the presence of long-range correlations for slow ramps and validates prior work [13]: the scaling is consistent with the expected KZ power law ($\xi \sim \Gamma^{-0.5}$) in a regime of intermediate ramp speeds. The data at both ends of the ramping rate range deviates from expected scaling. For fast ramps, the adiabaticity fails at both sides of the critical fan fails, and the correlation length saturates towards a single-site value, while for very slow ramps, the assumption that the system becomes frozen near criticality breaks down due to a finite-size gap in the system [3, 39]. We note, however, that the independent-defect theory, which predicts Poisson-binomial statistics, is expected to hold despite deviations from Kibble-Zurek scaling [19, 23, 24].

Next, we directly test the independent-defect theory by measuring its most readily accessible experimental prediction: the defect number variance being proportional,

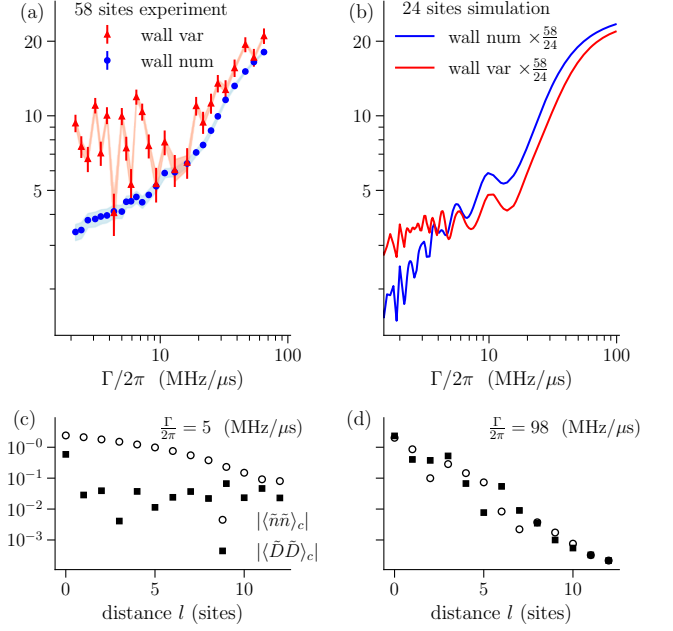


FIG. 3. Anomaly in the defect counting statistics. Domain wall mean (blue) and variance (red) vs the quench rate Γ from (a) experiments and (b) numerical simulations rescaled by the size ratio 58/24. The vertical error bars denote experimental statistical errors, and the bands denote the systematic errors due to zero-readout noise mitigation. In both experiments and numerics, we observe a salient regime at lower quench rates where the defect variance exceeds the mean. The discrepancy is associated with the development of non-trivial defect correlations. In numerics, we compare the connected correlators of the density-density and defect-defect observables: (c) for slow ramps, domain walls are anticorrelated, coinciding with a statistics anomaly; (d) at faster ramps, domain wall correlations simply follow the correlation length determined by density correlations.

and smaller than, the mean number of defects. The number of defects can be directly evaluated from two-point nearest-neighbor correlations that capture two types of domain walls ('00' and '11') on top of the antiferromagnetic phase:

$$\langle D \rangle = \sum_i \langle D_i \rangle = \sum_i \langle n_i n_{i+1} + (1 - n_i)(1 - n_{i+1}) \rangle. \quad (2)$$

The variance follows from four-point density correlators $\text{var } D = \langle D^2 \rangle - \langle D \rangle^2$. In contrast to the readout-robust correlation length, the defect number and variance are significantly affected by the readout error, which is skewed $\sim 5\%$ towards $|r_j\rangle \rightarrow |g_j\rangle$ misdetection. To recover reliable estimates of defect distribution moments, we carefully calibrate the readout error [33] during our data collection and apply zero-noise extrapolation during postprocessing [38]. The uncertainty in the calibration and mitigation procedure leads to a sizable systematic error, which we include in addition to the standard shot-distribution-derived error estimates.

Our main experimental results are summarized in Fig. 3(a). The number of domain walls consistently increases with the ramp speed, as expected from the correlation length result, given that $\langle D \rangle \propto \xi^{-1}$. For faster ramps, $\Gamma/2\pi \gtrsim 10$ MHz/ μ s, the defect number variance roughly matches the mean, within experimental uncertainties, in agreement with independent-defect theory. At ramps slower than $\Gamma/2\pi \sim 10$ MHz/ μ s, however, we observe an anomaly with the variance becoming larger than the mean. For the slowest ramps, the ratio $\text{var } D / \langle D \rangle \sim 3$ and lies well outside the error bounds, thus soundly contradicting independent-defect theory.

To exclude the experimental noise as the potential source of the anomaly, we perform exact diagonalization simulations [40] of our ramp protocol with up to 24 sites [38]. The main results are presented in Fig. 3(b) and exhibit the same qualitative behavior as the experiments: the fast ramp regime has $\text{var } D / \langle D \rangle$ constant – at slightly less than 1 – while the slow ramp regime shows a clear anomaly $\text{var } D > \langle D \rangle$. The quantitative behavior is in approximate agreement, including the value of the crossover ramp rate, with discrepancies likely due to the blockade subspace approximation [38], system size difference, and experimental noise. The simulation permits a finer look into defect-defect correlations [see Fig. 3(c,d)], which is hindered in experiment by prohibitive shot requirements. Tellingly, the defect-defect correlation behavior is distinct in the two regimes. In the “normal” fast ramp regime, the defect correlations follow the density correlations and decay with the same correlation length, corroborating the picture of independent defect mergers at the correlation length scale. In the anomalous regime, true defect correlations are established independent of density-density correlations; specifically, a defect suppresses the formation of other defects in its vicinity.

The anomaly in the defect statistics calls for a mechanism that produces correlated defects. We conjecture that this mechanism is related to non-critical coarsening dynamics that apply after the critical point is crossed [30–32]. Indeed, in sufficiently fast ramps, the Poissonian statistics prevails and the defects are formed by independent mergers in the vicinity of the critical points [see Fig. 1(a)]. The resulting non-critical coarsening proceeds on the typical timescale determined by the inverse gap [15, 32], with ramp time spent in the ordered phase being too brief to introduce defect correlations for fast ramps. In contrast, for slow ramps, the anomalous behavior directly follows, since the system spends a long time beyond the critical fan, and defect correlations can develop through coarsening, manifesting directly in the counting statistics [Fig. 1(b)].

The proposed quantum non-critical coarsening dynamics provides a general mechanism capable of generating defect correlations and anomalous statistics. We note, however, two alternative mechanisms that could also produce the anomaly, but are inconsistent with our obser-

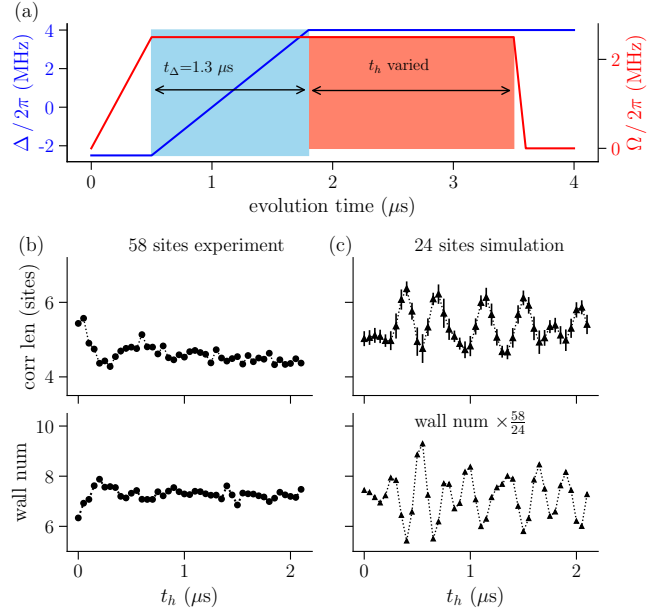


FIG. 4. **Hold protocol and dynamics.** (a) By appending the time constant protocol for a hold time t_h after the ramp, we probe the non-critical dynamics at fixed energy. Both in (b) experiment and (c) simulations, correlation lengths and domain wall numbers are stable in time, indicating a freeze out of the coarsening dynamics. Simulations further recover oscillatory behavior absent in experiments due to dephasing.

vations. First, long-range interactions are known to introduce an anomaly in the defect distributions, with no classical analog [27]. In particular, long-range interactions, which decay more slowly than r^{-d} (d is the system dimension), directly correlate defects during their formation. However, this does not apply to our $d = 1$ experiments. Second, the anomaly could arise classically in an independent-defect framework for an even-Poisson distribution, stemming from the constraint on pairwise defect formation [20]. Such a constraint commonly arises from topology and is indeed present in our system with periodic boundary conditions [38]. Our experimental and numerical results, however, disagree with the implications of even-Poisson theory. This theory predicts that the sizable anomaly $\text{var } D > \langle D \rangle$ in the slow ramp regime is followed by an increasing (doubling) slope of both the variance and the mean, while the opposite (flattening and slowdown of decay) is observed in the experiment and simulations. Additionally, it predicts that $\text{var } D > \langle D \rangle$ is valid at all ramp speeds, with exponential convergence between the variance and mean for fast ramps. This is also explicitly violated in fast-ramp numerics, while remaining ambiguous in experiments.

Finally, we devise and perform experiments to further probe and control the non-critical coarsening dynamics. The hold protocol, showcased in Fig. 4(a), consists of a fixed, intermediate speed ramp followed by a constant Hamiltonian evolution for different hold times

(t_h). This approach is equivalent to the hold protocol recently used to probe coarsening dynamics of the two-dimensional Rydberg Hamiltonian [15]. The correlation length and defect number are measured as a function of hold time, with experimental and simulated results presented in Figs. 4(b) and (c).

The hold dynamics exhibit constant correlation length and defect number on average in both the experiments and simulations. Furthermore, the numerics resolve the secondary effect of coherent oscillations in correlation length, with the period governed by the ground state energy gap [38], akin to the observations in two-dimensions [15]. These oscillations are absent in the experiment, likely due to dephasing [17, 33]. The freezing of correlation growth through coarsening is a surprising result, in sharp contrast with the observations in two-dimensions of diffusive correlation length growth, $\xi \propto t^{0.5}$ [15]. It showcases the level of control over coarsening dynamics that could be employed in future experiments to tune the appearance and properties of the defect statistics anomaly.

The independent-defect hypothesis [18, 19] provides a clear organizing principle for defect statistics, yet our data show that the conditions for its validity are subtle in quantum non-integrable systems: post-critical time scales and coarsening dynamics can generate correlated defects with anomalous statistics. Numerics corroborate that the effect is physical rather than noise-induced. By halting energy injection while maintaining a coherent drive in the hold experiments, we demonstrate control over the coarsening and observe an unexpected freezing of correlations, in sharp contrast to diffusive growth reported in two dimensions on similar platforms [15]. The mechanism for this coarsening freeze-out might include prethermalization [41–43] due to an energy scale separation deep in the ordered phase [17]. Alternatively, it could stem from the sensitivity of one-dimensional systems [36, 44] to experimental atom position disorder, which was already found to slow down ballistic correlation spreading to a diffusive one in the integrable case [45]. These results open a broader program to map the quantum defect statistics anomaly across dimensions, drive protocols, and disorder strengths, thus testing targeted predictions, including the scaling of higher cumulants, the hold- and ramp-time dependence of the anomaly, and the nature of induced defect correlations. More generally, such custom experimental probes would delineate the limits of Kibble–Zurek universality.

We acknowledge helpful discussions with Michael Koldrubetz and Fernando Gómez-Ruiz. This research was supported by the U.S. Department of Energy (DOE) under Contract No. DE-AC02-05CH11231, through the National Energy Research Scientific Computing Center (NERSC), an Office of Science User Facility located at Lawrence Berkeley National Laboratory.

* These authors contributed equally.

†Email address: balewski@lbl.gov; alehud@bu.edu; kklymko@lbl.gov; dcamps@lbl.gov; mkorn-jaca@quera.com.

- [1] T. W. B. Kibble, Topology of cosmic domains and strings, *Journal of Physics A: Mathematical and General* **9**, 1387 (1976).
- [2] W. H. Zurek, Cosmological experiments in superfluid helium?, *Nature* **317**, 505 (1985).
- [3] J. Dziarmaga, Dynamics of a quantum phase transition and relaxation to a steady state, *Advances in Physics* **59**, 1063–1189 (2010).
- [4] I. Chuang, R. Durrer, N. Turok, and B. Yurke, Cosmology in the laboratory: defect dynamics in liquid crystals, *Science* **251**, 1336 (1991).
- [5] R. Monaco, J. Mygind, R. J. Rivers, and V. P. Koshelets, Spontaneous fluxoid formation in superconducting loops, *Physical Review B* **80**, 180501 (2009).
- [6] C. N. Weiler, T. W. Neely, D. R. Scherer, A. S. Bradley, M. J. Davis, and B. P. Anderson, Spontaneous vortices in the formation of Bose–Einstein condensates, *Nature* **455**, 948 (2008).
- [7] K. Pyka, J. Keller, H. L. Partner, R. Nigmatullin, T. Burgermeister, D. M. Meier, K. Kuhlmann, A. Retzker, M. B. Plenio, P. Zoller, F. Schmidt-Kaler, and U. G. Poschinger, Topological defect formation and spontaneous symmetry breaking in ion Coulomb crystals, *Nature Communications* **4**, 2291 (2013).
- [8] S. Ulm, J. Roßnagel, G. Jacob, C. Degünther, S. T. Dawkins, U. G. Poschinger, R. Nigmatullin, A. Retzker, M. B. Plenio, F. Schmidt-Kaler, and K. Singer, Observation of the Kibble–Zurek scaling law for defect formation in ion crystals, *Nature Communications* **4**, 2290 (2013).
- [9] K. Xu, J. Zhang, X. Peng, N. Rajendran, J. Chu, and J. Du, Simulating the Kibble–Zurek mechanism of the Ising model with a superconducting qubit system, *Scientific Reports* **6**, 22667 (2016).
- [10] Y. Bando, H. Nishimori, T. Albash, D. A. Lidar, S. Suzuki, and A. del Campo, Probing the universality of topological defect formation in a quantum annealer: Kibble–Zurek mechanism and beyond, *Physical Review Research* **2**, 033369 (2020).
- [11] K. Du, X. Fang, C. Won, C. De, F.-T. Huang, W. Xu, H. You, F. J. Gómez-Ruiz, A. del Campo, and S.-W. Cheong, Kibble–Zurek mechanism of Ising domains, *Nature Physics* **19**, 1495 (2023).
- [12] H. Bernien, S. Schwartz, A. Keesling, H. Levine, A. Omran, H. Pichler, S. Choi, A. S. Zibrov, M. Endres, M. Greiner, V. Vuletić, and M. D. Lukin, Probing many-body dynamics on a 51-atom quantum simulator, *Nature* **551**, 579 (2017).
- [13] A. Keesling, A. Omran, H. Levine, H. Bernien, H. Pichler, S. Choi, R. Samajdar, S. Schwartz, P. Silvi, S. Sachdev, P. Zoller, M. Endres, M. Greiner, V. Vuletić, and M. D. Lukin, Quantum Kibble–Zurek mechanism and critical dynamics on a programmable Rydberg simulator, *Nature* **568**, 207 (2019).
- [14] S. Ebadi, T. T. Wang, H. Levine, A. Keesling, G. Semeghini, A. Omran, D. Bluvstein, R. Samajdar, H. Pichler, W. W. Ho, S. Choi, S. Sachdev, M. Greiner, V. Vuletić, and M. D. Lukin, Quantum phases of matter

- on a 256-atom programmable quantum simulator, *Nature* **595**, 227 (2021).
- [15] T. Manovitz, S. H. Li, S. Ebadi, R. Samajdar, A. A. Geim, S. J. Evered, D. Bluvstein, H. Zhou, N. U. Koyluoglu, J. Feldmeier, P. E. Dolgirev, N. Maskara, M. Kalinowski, S. Sachdev, D. A. Huse, M. Greiner, V. Vuletić, and M. D. Lukin, Quantum coarsening and collective dynamics on a programmable quantum simulator, *Nature* **635**, 278 (2024).
 - [16] M. R. Hirsbrunner, M. Kornjača, R. Samajdar, S. Darbha, M. Hamdan, J. Balewski, E. Rrapaj, S.-T. Wang, D. Camps, F. Liu, P. L. S. Lopes, and K. Klymko, Quantum criticality and nonequilibrium dynamics on a Lieb lattice of Rydberg atoms (2025), [arXiv:2508.05737 \[cond-mat.quant-gas\]](#).
 - [17] S. Darbha, A. Khudorozhkov, P. L. S. Lopes, F. Liu, E. Rrapaj, J. Balewski, M. Hamdan, P. E. Dolgirev, A. Schuckert, K. Klymko, S.-T. Wang, M. D. Lukin, D. Camps, and M. Kornjača, Probing emergent prethermal dynamics and resonant melting on a programmable quantum simulator (2025), [arXiv:2510.11706 \[quant-ph\]](#).
 - [18] A. del Campo, Universal statistics of topological defects formed in a quantum phase transition, *Physical Review Letters* **121**, 200601 (2018).
 - [19] F. J. Gómez-Ruiz, J. J. Mayo, and A. del Campo, Full counting statistics of topological defects after crossing a phase transition, *Physical Review Letters* **124**, 240602 (2020).
 - [20] A. del Campo, F. J. Gómez-Ruiz, Z.-H. Li, C.-Y. Xia, H.-B. Zeng, and H.-Q. Zhang, Universal statistics of vortices in a newborn holographic superconductor: beyond the Kibble–Zurek mechanism, *Journal of High Energy Physics* **2021**, 61 (2021).
 - [21] F. J. Gómez-Ruiz, D. Subires, and A. del Campo, Role of boundary conditions in the full counting statistics of topological defects after crossing a continuous phase transition, *Physical Review B* **106**, 134302 (2022).
 - [22] A. del Campo, F. J. Gómez-Ruiz, and H.-Q. Zhang, Locality of spontaneous symmetry breaking and universal spacing distribution of topological defects formed across a phase transition, *Phys. Rev. B* **106**, L140101 (2022).
 - [23] A. del Campo, H.-B. Zeng, C.-Y. Xia, and Z.-H. Li, Universal breakdown of Kibble–Zurek scaling in fast quenches across a phase transition, *Physical Review Letters* **130**, 060402 (2023).
 - [24] J.-M. Cui, F. J. Gómez-Ruiz, Y.-F. Huang, C.-F. Li, G.-C. Guo, and A. del Campo, Experimentally testing quantum critical dynamics beyond the Kibble–Zurek mechanism, *Communications Physics* **3**, 44 (2020).
 - [25] O. Kiss, D. Teplitskiy, M. Grossi, and A. Mandarino, Statistics of topological defects across a phase transition in a superconducting quantum processor, *Quantum Science and Technology* **10**, 035037 (2025).
 - [26] M. Kolodrubetz, D. Pekker, B. K. Clark, and K. Sengupta, Nonequilibrium dynamics of bosonic Mott insulators in an electric field, *Phys. Rev. B* **85**, 100505 (2012).
 - [27] S. Gherardini, L. Buffoni, and N. Defenu, Universal defects statistics with strong long-range interactions, *Phys. Rev. Lett.* **133**, 113401 (2024).
 - [28] K. Roychowdhury, R. Moessner, and A. Das, Dynamics and correlations at a quantum phase transition beyond Kibble–Zurek, *Physical Review B* **104**, 014406 (2021).
 - [29] M. Mattioli, N. Defenu, C. Ricci, and S. Ruffo, Defect production across higher-order phase transitions beyond Kibble–Zurek, *Physical Review Letters* **134**, 010409 (2025).
 - [30] A. J. Bray, Theory of phase-ordering kinetics, *Advances in Physics* **43**, 357 (1994).
 - [31] A. J. Bray, Coarsening dynamics of phase-separating systems, *Philosophical Transactions of the Royal Society A* **361**, 781 (2003).
 - [32] R. Samajdar and D. A. Huse, Quantum and classical coarsening and their interplay with the Kibble–Zurek mechanism (2024), [arXiv:2401.15144 \[quant-ph\]](#).
 - [33] J. Wurtz, A. Bylinskii, B. Braverman, J. Amato-Grill, S. H. Cantu, F. Huber, A. Lukin, F. Liu, P. Weinberg, J. Long, S.-T. Wang, N. Gemelke, and A. Keesling, Aquila: Quera’s 256-qubit neutral-atom quantum computer (2023), [arXiv:2306.11727 \[quant-ph\]](#).
 - [34] P. Weinberg, K.-H. Wu, J. Long, and X.-z. R. Luo, *Quera computing/bloqade-python: v0.15.11* (2024).
 - [35] J. Zhang, S. H. Cantú, F. Liu, A. Bylinskii, B. Braverman, F. Huber, J. Amato-Grill, A. Lukin, N. Gemelke, A. Keesling, S.-T. Wang, Y. Meurice, and S.-W. Tsai, Probing quantum floating phases in Rydberg atom arrays, *Nature Communications* **16**, 712 (2025).
 - [36] S. Sachdev, *Quantum Phase Transitions*, 2nd ed. (Cambridge University Press, 2011).
 - [37] K. Sengupta, S. Powell, and S. Sachdev, Quench dynamics across quantum critical points, *Phys. Rev. A* **69**, 053616 (2004).
 - [38] See Supplementary Information below.
 - [39] M. Kolodrubetz, B. K. Clark, and D. A. Huse, Nonequilibrium dynamic critical scaling of the quantum Ising chain, *Phys. Rev. Lett.* **109**, 015701 (2012).
 - [40] *Bloqade.jl: Package for the quantum computation and quantum simulation based on the neutral-atom architecture.* (2023).
 - [41] J. Berges, S. Borsányi, and C. Wetterich, Prethermalization, *Phys. Rev. Lett.* **93**, 142002 (2004).
 - [42] M. Moeckel and S. Kehrein, Interaction quench in the hubbard model, *Phys. Rev. Lett.* **100**, 175702 (2008).
 - [43] T. Mori, T. N. Ikeda, E. Kaminishi, and M. Ueda, Thermalization and prethermalization in isolated quantum systems: a theoretical overview, *Journal of Physics B: Atomic, Molecular and Optical Physics* **51**, 112001 (2018).
 - [44] D. A. Abanin, E. Altman, I. Bloch, and M. Serbyn, Colloquium: Many-body localization, thermalization, and entanglement, *Rev. Mod. Phys.* **91**, 021001 (2019).
 - [45] C. B. Dag, H. Ma, P. M. Eugenio, F. Fang, and S. F. Yelin, Emergent disorder and sub-ballistic dynamics in quantum simulations of the Ising model using Rydberg atom arrays (2025), [arXiv:2411.13643 \[quant-ph\]](#).
 - [46] R. Majumdar, P. Rivero, F. Metz, A. Hasan, and D. S. Wang, Best practices for quantum error mitigation with digital zero-noise extrapolation (2023), [arXiv:2307.05203 \[quant-ph\]](#).
 - [47] S. Bravyi, S. Sheldon, A. Kandala, D. C. McKay, and J. M. Gambetta, Mitigating measurement errors in multiqubit experiments, *Phys. Rev. A* **103**, 042605 (2021).
 - [48] *Perlmutter.* (2023).

Supplementary Information: “Observation of an anomaly in the statistics of Kibble-Zurek defects”

In this supplementary information, we present the details of readout error mitigation and error estimation procedures in Sec. S1. The additional numerical results follow, including the calculation details (Sec. S2A), the effect of the perfect blockade constraint (Sec. S2B), details of defect correlations and statistics (Sec. S2C), and supplementary hold dynamics results presenting the spectrum of defect density oscillations (Sec. S2D).

S1. READOUT ERROR MITIGATION

The measurement of defect counting statistics in one-dimensional Rydberg atom chains relies on accurately determining the state of each atom at the end of the evolution, as the defect number is sensitive to readout errors. In our experiments, the dominant sources of readout errors are finite detection fidelity during fluorescence imaging and Rydberg state decay during the comparatively long imaging time [33], which manifest as state-dependent bit-flip errors. Each experimental shot yields a fluorescence image of the atom chain, which is thresholded to produce a binary string identifying ground ($|0\rangle$) and excited ($|1\rangle$) states [33]. From these measured bitstrings, we extract defect-relevant observables by counting domain wall defects, which correspond to “00” and “11” patterns. Any readout error can introduce these patterns, leading to a systematically increased domain wall count and a biased variance.

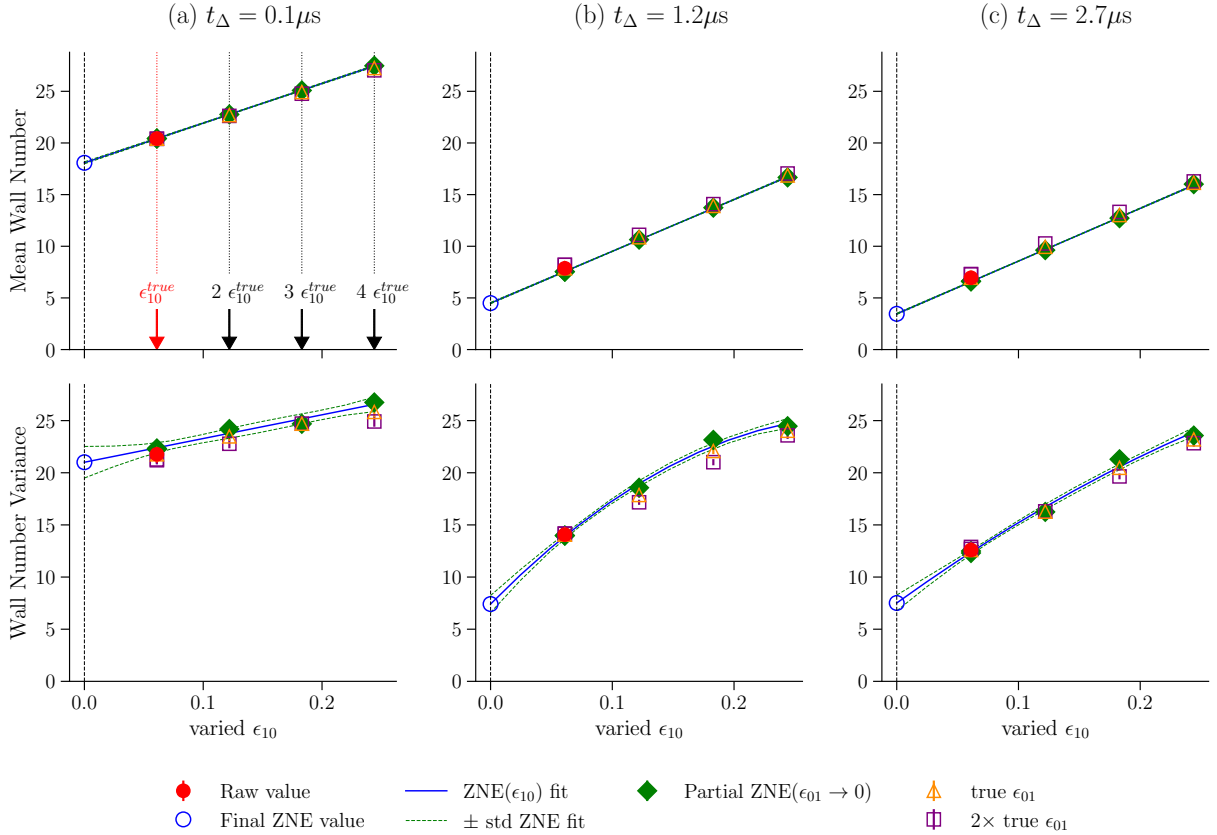


FIG. 5. Zero-noise extrapolation (ZNE) for readout error mitigation. The two-step ZNE procedure is shown for the mean wall number (top row) and wall number variance (bottom row) at three different ramp times t_Δ (columns a-c). The process starts with raw experimental data (red circle at $\epsilon_{10}^{\text{true}}$) and data points where noise has been artificially amplified (orange triangles and purple squares). First, a linear extrapolation in the ϵ_{01} error is performed for fixed values of ϵ_{10} to obtain the partially-mitigated intermediate data (green diamonds). Second, these intermediate points are extrapolated to the zero-noise limit ($\epsilon_{10} \rightarrow 0$). A linear model (blue line) is sufficient for the mean wall number, while a quadratic model is required for the variance. The final, fully error-mitigated value is the extrapolated point at $\epsilon_{10} = 0$ (blue open circle). The dashed green lines represent the one-standard-deviation confidence interval of the fit.

To mitigate the impact of readout errors, we employ zero-noise extrapolation (ZNE). While ZNE is commonly used in quantum computing to suppress gate errors, a process that typically requires deliberately adding noise and

performing additional experiments [46], our protocol is tailored to exclusively correct readout errors. This allows us to perform ZNE entirely as a post-processing step on the measured data, without any additional experimental overhead, as long as the readout error probabilities are reliably and independently inferred from dedicated calibration experiments.

To account for potential hardware drift over data-taking sessions lasting several hours, we calibrate the readout errors both before and after the main experiment. Using the standard method of fitting damped Rabi oscillations [33], we measure the probability of misclassifying a true Rydberg state as ground (ϵ_{10}) and a true ground state as Rydberg (ϵ_{01}). The average values over the calibrations passes were $\epsilon_{10}^{\text{true}} = 0.061 \pm 0.004$ and $\epsilon_{01}^{\text{true}} = 0.009 \pm 0.002$, with the uncertainties reflecting the difference between the passes. Qubits are spatially isolated and identical atoms that are imaged simultaneously; thus, no higher-order correlated readout error channels appear, making our two-parameter readout error model complete.

We implement ZNE in the two-dimensional space spanned by the error parameters ($\epsilon_{01}, \epsilon_{10}$) through noisy resampling. The procedure involves artificially amplifying the noise in the measured bitstrings by randomly flipping bits with probabilities corresponding to multiples of the calibrated error rates, ($\alpha\epsilon_{01}^{\text{true}}, \beta\epsilon_{10}^{\text{true}}$). For each pair of noise amplification factors (α, β), we recalculate the average wall number and variance on the resampled bitstring distribution. For both observables their statistical errors were computed as well. To reduce the statistical uncertainty, the sampling was performed four times, and the results were averaged.

Since $\epsilon_{01}^{\text{true}}$ is very small, we factorize the two-dimensional extrapolation into two steps, as illustrated in Fig. 5. First, for several fixed multiples of ϵ_{10} , we apply a linear extrapolation over ϵ_{01} to mitigate the small $\epsilon_{01}^{\text{true}}$ error by regressing it to zero. The results of this initial step are shown as green diamonds. Second, using these intermediate points, we assume a model for ϵ_{10} dependence, fit it, and perform an extrapolation to the $\epsilon_{10} \rightarrow 0$ limit. For the wall number (top row), a linear fit is sufficient across all ramp times t_{Δ} . For the wall variance (bottom row), the data exhibit clear curvature, calling for a quadratic extrapolation. The final, fully mitigated values are shown as blue circles.

The ZNE models are chosen based on the observed data trends. The linear model for the wall number explains well the ϵ_{10} dependence for all t_{Δ} , with the relative ZNE correction increasing with t_{Δ} while the extrapolation error remains small. The linear model for wall number is also fully consistent with the commonly employed confusion-matrix-inversion-based readout mitigation [47]. It is evident that the linear model does not capture the trend observed in the experimentally measured wall variance data shown in the bottom row of Fig. 5, particularly at intermediate t_{Δ} . This observation supports our choice of a quadratic fit model. Furthermore, both a linear ZNE model and confusion matrix inversion for the wall variance fail when tested on synthetic data.

The ZNE fit was performed on observables weighted by their statistical errors; thus, the uncertainty in the extrapolated final values already reflects the statistical uncertainty of the raw bitstring distribution. This uncertainty of the extrapolation is represented by the one-standard-deviation bands (dashed green lines). For the wall variance, the uncertainty grows significantly as $\epsilon_{10} \rightarrow 0$ because the noise model is quadratic in $\epsilon_{10} - \epsilon_{10}^{\text{true}}$. This uncertainty is propagated to the final results presented in the main text.

The ZNE procedure described above yields corrected observable values along with their associated statistical errors. In addition, we estimated the systematic error introduced by the ZNE correction itself. The two input parameters $\epsilon_{10}^{\text{true}}$ and $\epsilon_{01}^{\text{true}}$ determine the output of the ZNE postprocessing, and each is known with an uncertainty $\delta\epsilon_{10}^{\text{true}}$ and $\delta\epsilon_{01}^{\text{true}}$, respectively. To assess the impact of these uncertainties, we repeated the ZNE estimation process an additional four times, each time assuming $\tilde{\epsilon}_{10}^{\text{true}}$ and $\tilde{\epsilon}_{01}^{\text{true}}$ to be $\epsilon_{10}^{\text{true}} \pm \delta\epsilon_{10}^{\text{true}}$ and $\epsilon_{01}^{\text{true}} \pm \delta\epsilon_{01}^{\text{true}}$, respectively. For each ramp time t_{Δ} , we computed the maximum deviation between the baseline ZNE result and the four variant ZNE results obtained with perturbed ϵ values by $\pm\delta\epsilon$. This maximum deviations at every t_{Δ} are reported as the systematic errors for the final observables and are shown in Figs. 3(a) and (b) as orange and blue bands, respectively.

S2. SUPPLEMENTARY NUMERICAL RESULTS

A. Numerical Methods

The numerical simulations of the Rydberg atom chain we performed using exact diagonalization (ED), implemented in Julia via the open-source package `Bloqade.jl` [40]. All simulations are executed on the Perlmutter supercomputer [48] at the National Energy Research Scientific Computing Center (NERSC), hosted at Lawrence Berkeley National Laboratory. Two types of calculations are performed: (i) projected within the Rydberg blockaded Hilbert subspace, allowing access to system sizes up to $L = 24$ atoms, and (ii) in the full Hilbert space, with chains of up

to $L = 20$ atoms. This ED-based approach enables us to compute the exact many-body wavefunction and obtain numerically exact time-evolution data for all observables of interest.

The atomic spacing is fixed at $a = 6.2 \mu\text{m}$, corresponding to a dimensionless blockade ratio $R_b/a = 1.35$, where the blockade radius is $R_b = (C_6/\Omega)^{1/6}$, with the van der Waals coefficient $C_6/2\pi = 862690 \text{ MHz} \cdot \mu\text{m}^6$ and the maximal Rabi frequency set to $\Omega_{\text{max}}/2\pi = 2.5 \text{ MHz}$. The Hamiltonian (Eq. 1) is explicitly time-dependent, with the Rabi frequency $\Omega(t)$ and detuning $\Delta(t)$ temporal profiles the same as in Fig. 2(b) and Fig. 4(a). In particular, $\Omega(t)$ features a rapid initial ramp-up and final ramp-down of duration $0.5 \mu\text{s}$ each, while $\Delta(t)$ is linearly swept from $\Delta_{\text{min}}/2\pi = -2.5 \text{ MHz}$ to $\Delta_{\text{max}}/2\pi = 4.0 \text{ MHz}$ over a total ramp time $t_\Delta \in [0.066, 32.5] \mu\text{s}$.

All simulations are initialized in the fully unexcited product state $|0\rangle^{\otimes L}$, and only the final state at the end of the evolution is stored for analysis. Observables, including the domain-wall density, its variance, and correlation functions, are computed from this final state. Whenever correlation functions are evaluated, we use the shifted Ising variables, $\tilde{n}_i \equiv 2(n_i - \frac{1}{2})$, $\tilde{D}_i \equiv 2(D_i - \frac{1}{2})$, whose eigenvalues are ± 1 . This choice centers the observables around zero and facilitates comparison between different quantities. All reported correlation functions are connected, i.e. computed as $\langle AB \rangle_c \equiv \langle AB \rangle - \langle A \rangle \langle B \rangle$, and are shown as absolute values throughout.

B. Effect of the Blockade Subspace

To assess the role of the Rydberg blockade constraint in the observed dynamics, we compare numerical simulations performed in the full Hilbert space, where blockade violations are allowed, to those restricted to the blockade subspace, where adjacent atoms cannot be simultaneously excited. Panels (a) and (b) in Fig. 6 compare these two approaches. We show the average number of domain walls $\langle D \rangle$ and its variance $\langle D^2 \rangle - \langle D \rangle^2$ as a function of the effective sweep rate $\Gamma/2\pi$ for a chain of $L = 20$ atoms with periodic boundary conditions (PBC).

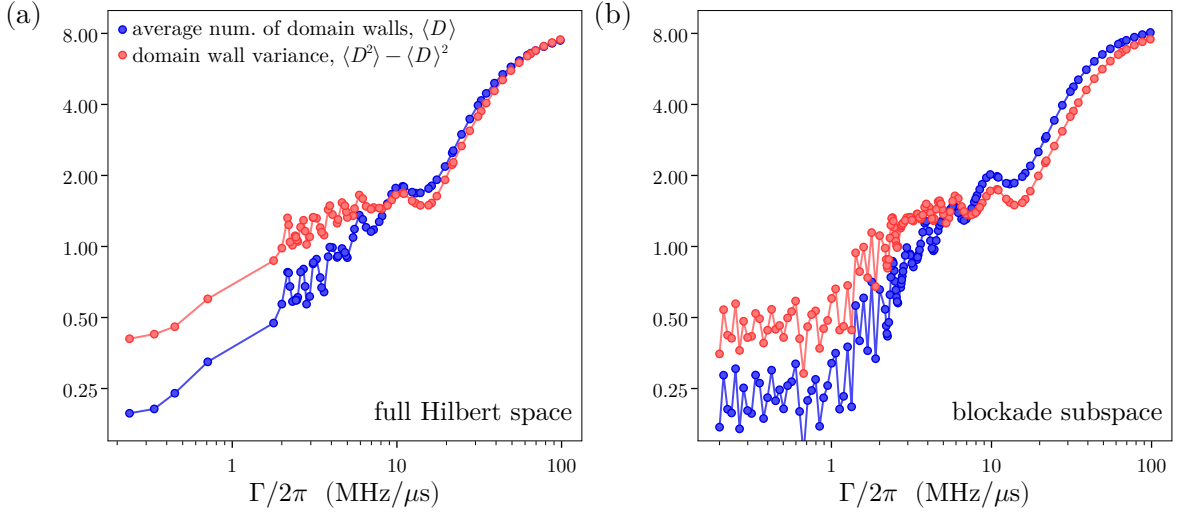


FIG. 6. **Effect of using the blockade subspace.** Average domain wall number $\langle D \rangle$ (blue) and its variance $\langle D^2 \rangle - \langle D \rangle^2$ (red) for a chain of $L = 20$ atoms with periodic boundary conditions (PBC), obtained via exact diagonalization. (a) Results computed in the full 2^L -dimensional Hilbert space. (b) Results restricted to the blockade subspace, where neighboring atoms cannot simultaneously occupy the Rydberg state.

The overall behavior of both observables is qualitatively similar in the two cases. For intermediate ramp rates Γ , the mean number of domain walls and their variance exhibit a sublinear Kibble-Zurek-like scaling, approximately following $\Gamma^{-1/2}$. At low Γ , both quantities saturate to constant values, with the variance larger than the mean. This consistency across the two Hilbert spaces demonstrates that the Kibble-Zurek statistics anomaly reported in the main text is not an artifact of restricting to the blockade subspace, but a robust feature of the many-body dynamics itself.

Quantitatively, the blockade constraint suppresses large fluctuations by reducing the accessible configuration space, in particular forbidding “11” domain wall configurations. Consequently, the variance in the blockade subspace, the numerical result reported in the main text, remains slightly lower than in the full Hilbert-space case, particularly at intermediate and high ramp rates where blockade-violating configurations are energetically suppressed but not entirely forbidden. At least part of the quantitative difference between the experiment and numerics reported in the

main text could be attributed to the blockade subspace constraint. These differences underscore the role of kinetic constraints in shaping excitation statistics, while confirming that blockade-violating processes do not qualitatively affect the anomalous scaling behavior.

C. Defect counting statistics and correlations

To gain further insight into the counting statistics of defects generated during the ramp, we analyze both the distribution of the total number of antiferromagnetic domain walls and their spatial correlations (Figs. 7–8). The probability distributions in Fig. 7 show the likelihood of observing a given number of domain walls for various ramp rates Γ , obtained via exact diagonalization within the blockade subspace. For slow ramps, the distributions deviate from the even Poisson form.

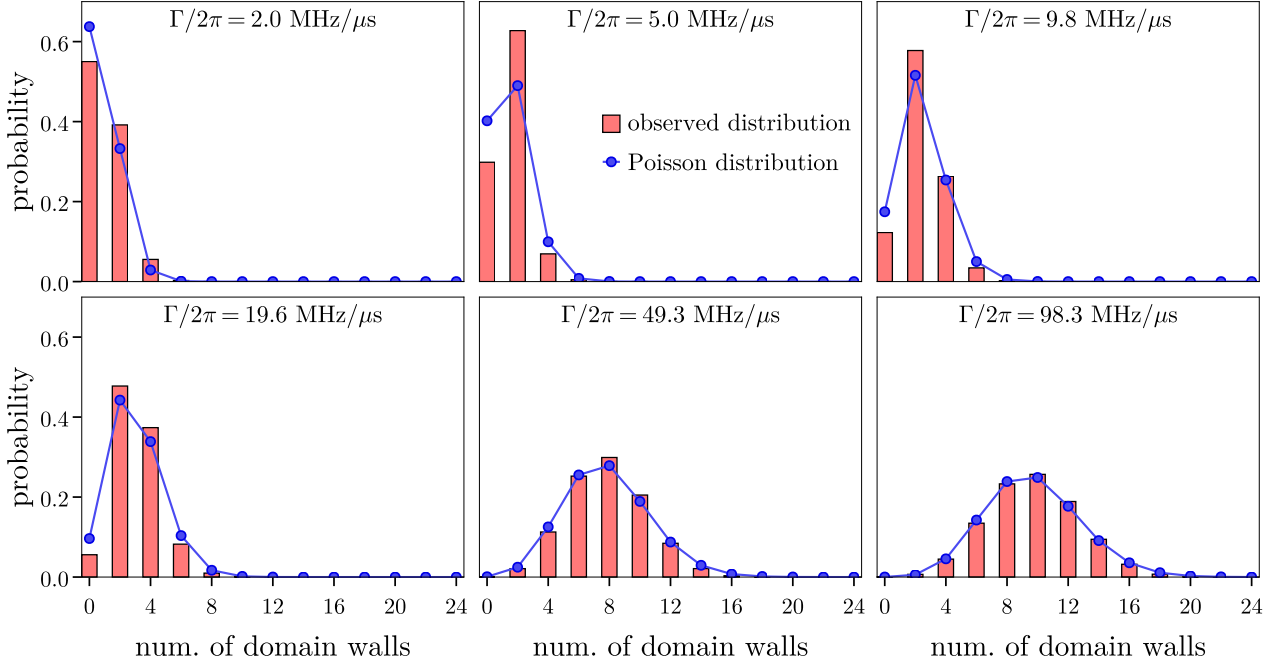


FIG. 7. **Defect number distribution.** (Red bars) Probability distribution of the number of domain walls for various ramp rates Γ , obtained numerically via exact diagonalization within the blockade subspace for a chain of $L = 24$ atoms with periodic boundary conditions. (Blue dots and lines) Corresponding normalized (even) Poisson distributions, $P(k) = \lambda^k e^{-\lambda} / k!$, with $\lambda = \langle D \rangle$ the average number of domain walls. Normalization is required since only even values of k are allowed with PBC.

As the ramp rate increases, the distributions broaden and gradually approach the Poisson distribution, $P(k \in \text{even}) \propto \lambda^k e^{-\lambda} / k!$, with $\lambda = \langle D \rangle$ the mean number of domain walls. At large Γ , the observed histograms coincide closely with the Poisson curves, indicating that the excitations are produced independently across the system. Note that because periodic boundary conditions enforce that domain walls appear in pairs, only even values of k are allowed, and the corresponding even Poisson distribution is renormalized accordingly.

The crossover from correlated to uncorrelated defect formation is further supported by the behavior of the connected density–density and domain-wall–domain-wall correlation functions shown in Fig. 8 (evaluated using the shifted Ising variables defined in the caption). At high Γ , the defect correlations decay exponentially with distance, following the correlation length determined by density correlations, reflecting the statistically independent defect formation from correlation-length-sized predomains. At low Γ , defect correlations deviate from density correlations, with the existence of a defect suppressing the formation of nearby defects. The deviations from the Poisson distribution and the correlated nature of the defects for slow ramps are two equivalent representations of the defect statistics anomaly we observe. As proposed in the main text, defects created during the critical passage of the fan undergo non-critical dynamics deep in the ordered phase, producing both non-trivial defect correlations and non-Poissonian counting statistics.

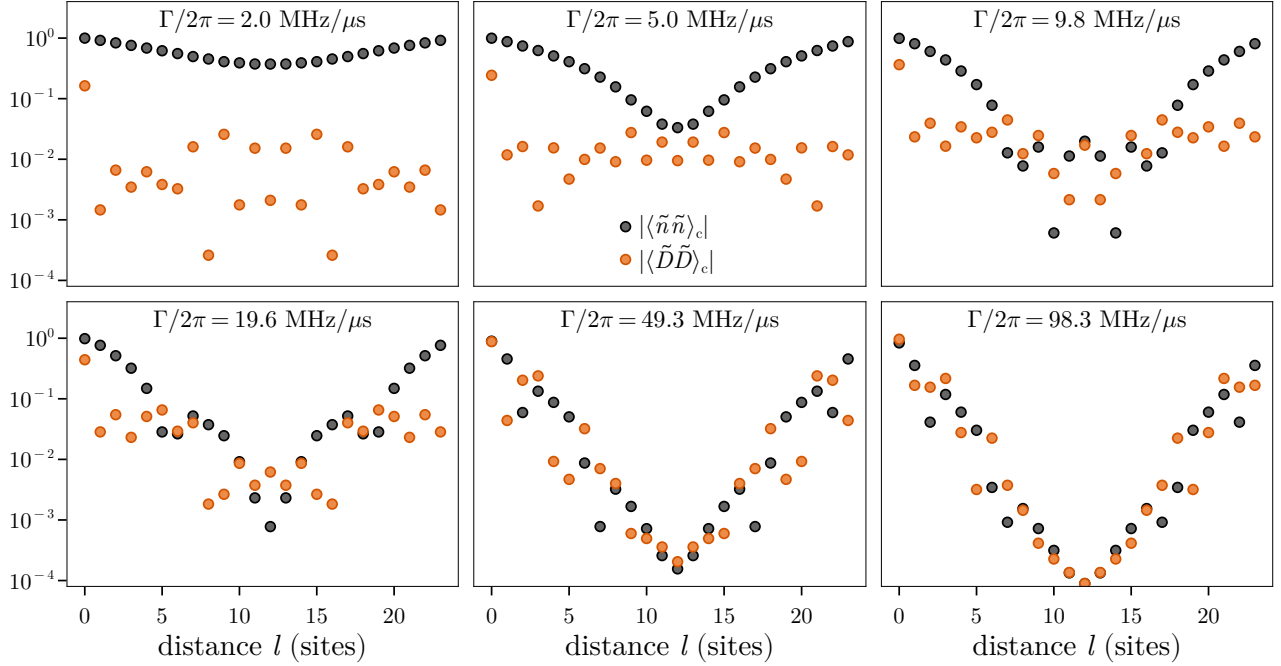


FIG. 8. **Correlation functions.** Absolute values of the connected correlation functions of the shifted Ising observables $\tilde{n}_i = 2(n_i - 1/2)$ (density, black) and $\tilde{D}_i = 2(D_i - 1/2)$ (domain wall, orange) for various ramp rates Γ , obtained numerically via exact diagonalization within the blockade subspace for a chain of $L = 24$ atoms with periodic boundary conditions.

D. Hold dynamics

To probe and control the non-critical dynamics in the ordered phase, we perform “hold” experiments in which the detuning is kept fixed at its final value after the ramp, and the system evolves under a time-independent Hamiltonian for a variable duration t_h (Fig. 9). The driving protocol and system geometry used for simulations are shown in Figs. 9(b)–(c). The evolution of the mean domain-wall number $\langle D \rangle$, its variance $\langle D^2 \rangle - \langle D \rangle^2$, and the density–density correlation length ξ during the hold stage is displayed in Fig. 9(a) for several ramp durations t_Δ , supplementing the main text results. As reported, all three observables are dominated by their constant running averages, in contrast to the diffusive growth observed in the 2D Rydberg array experiments of Ref. [15]. Coherent oscillations are superimposed on the main constant signal. The oscillations have well-defined frequencies, suggesting that the system evolves within a subset of low-lying many-body eigenstates.

The origin of the oscillations is manifest in their Fourier spectra, presented in Fig. 9(d). In all cases, the oscillation frequencies below the ground state energy gap (dashed lines) are strongly suppressed, with the dominant frequency coinciding with the first band of excitations starting just after $\nu = E_{\text{gap}}/(2\pi\hbar)$. The gap is calculated from the Hamiltonian at the final detuning (hold Hamiltonian). This demonstrates that the ramp prepares a superposition of the antiferromagnetic ground state and its several low-energy excited states in the ordered phase. The subsequent hold dynamics therefore correspond to coherent amplitude-mode oscillations across the system gap, directly analogous to the Higgs-related oscillations observed in 2D Rydberg arrays [15].

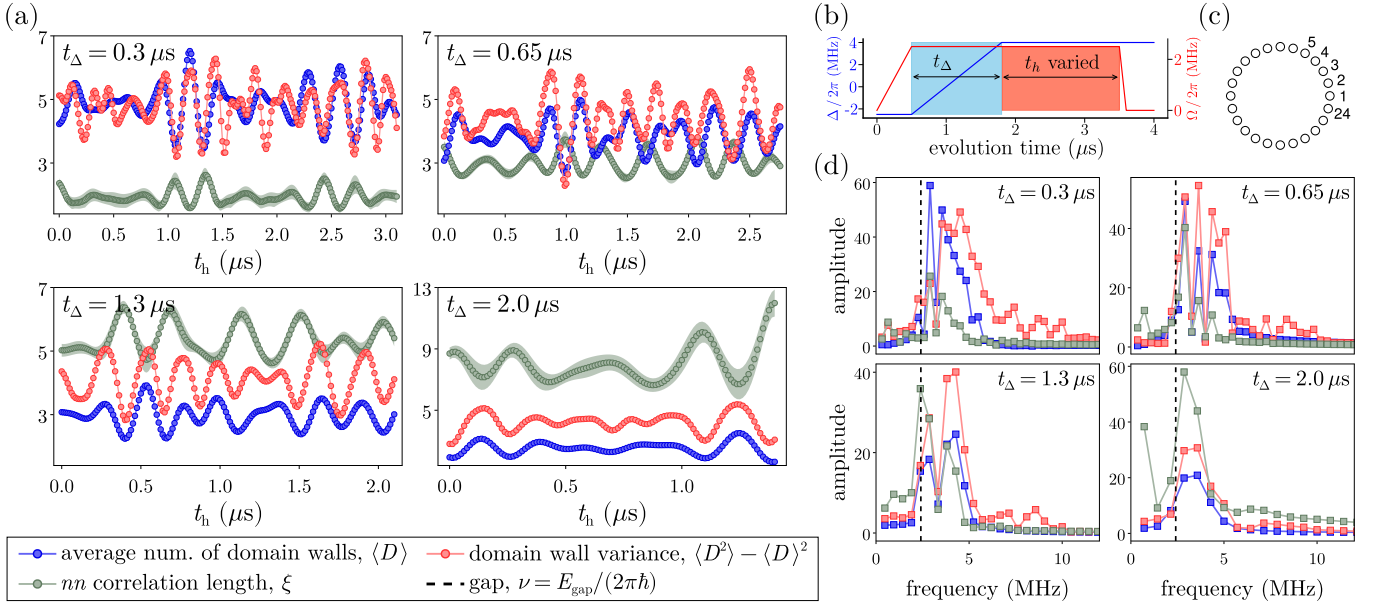


FIG. 9. **Hold dynamics spectrum in simulations.** (a) Time evolution of the average number of domain walls $\langle D \rangle$ (blue), its variance $\langle D^2 \rangle - \langle D \rangle^2$ (red), and the density–density correlation length ξ (green) during the hold stage of the experiment, for four different ramp durations t_Δ . The shaded green band denotes the standard error from fitting the correlation function with an exponential decay. (b) Driving fields used in the simulated protocol. (c) Geometry of the $L = 24$ atom chain with periodic boundary conditions. (d) Fourier transform of the time series in (a); the system’s spectral gap frequency $\nu = E_{\text{gap}}/(2\pi\hbar)$ is indicated by the black dashed line.